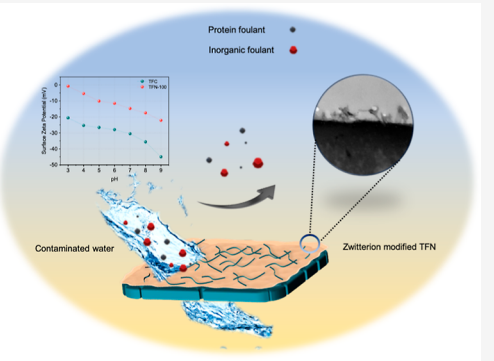
I&EC research
Industrial & Engineering Chemistry Research
pubs.acs.org/IECR
Article

Hydrophilic Antifouling Thin-Film Nanocomposite Forward Osmosis Membranes: Effect of Zwitterion-Functionalized Carbon Nanofiber Modification

Mehrasa Yassari, Alireza Shakeri,* Pooria Karami, and Mohtada Sadrzadeh

Cite This: *Ind. Eng. Chem. Res.* 2024, 63, 566−578
Read Online
ACCESS | Metrics & More | Article Recommendations

ABSTRACT: The polyamide (PA) active layer plays a key role in the permeation and antifouling properties of thin-film composite (TFC) membranes. In this study, we synthesized a nature-based zwitterionic thin-film nanocomposite (TFN) membrane with improved organic fouling resistance. Hydrophilic zwitterionic poly(sulfobetaine methacrylate) (PSBMA) was chemically introduced onto the surface of cellulose nanofibers (CNFs) to form CNF-*g*-PSBMA, which was subsequently incorporated into the PA selective layer. The cross-sectional transmission electron microscopy images and 3D atomic force microscopy surface topographies of synthesized TFC membranes showed that CNF-*g*-PSBMA led to the formation of a thinner and smoother PA layer. The performance of membranes was investigated in a forward osmosis (FO) filtration setup in two FO and pressure-retarded osmosis (PRO) modes. The water flux in FO and PRO modes showed an increase of 16.3 and 38 LMH, respectively, with a reverse salt flux similar to that of the pristine membrane. The modified TFN membranes revealed enhanced antifouling properties against sodium alginate and bovine serum albumin foulants up to four times compared with the unmodified TFC because of their improved hydrophilicity and smoother surface. The CNF-*g*-PSBMA-modified TFNs demonstrated great potential for use in FO filtration, thanks to the incorporation of nature-based green materials, which significantly enhanced the membrane performance.



1. INTRODUCTION

In recent years, the ever-growing population, global warming, and rapid industrialization have intensified concerns about freshwater scarcity. The vital need for clean water, which is expected to negatively affect nearly 4 billion people globally in the forthcoming decades, needs to be urgently addressed.[1] Feasible approaches to providing clean water are saline/brackish water desalination and wastewater treatment, recycling, and reuse via cost- and energy-efficient technologies.[2]

Membrane technology has found widespread applications in freshwater production and has emerged as an effective remedy for water scarcity. Current membrane processes, such as reverse osmosis (RO), electrodialysis, and membrane distillation, are energy-intensive.[3−6] In contrast, forward osmosis (FO) offers many advantages, such as lower energy consumption, less fouling tendency, and a reasonable water recovery rate, making it an excellent alternative to conventional processes.[7−9] To date, FO has been successfully employed in desalination,[10,11] wastewater treatment,[12,13] pharmaceutical industries,[14,15] food processing,[16,17] and osmotic power generation.[18,19]

In the FO process, water flows from the low osmotic potential side feed solution (FS) to the high osmotic pressure draw solution (DS) due to the natural osmotic pressure difference. A semipermeable membrane selectively allows the passage of water molecules and rejects the solutes.[20] Developing a high-performance semipermeable membrane is the key to the successful development of FO process. Currently, thin-film composite (TFC) membranes dominate the Global FO membrane market. A TFC membrane has a unique multilayer structure comprising a bottom porous polymeric support layer and a highly cross-linked top polyamide (PA) active layer, providing high water flux, salt rejection, and mechanical durability.[21,22]

The TFC membranes currently available on the market are primarily designed for RO applications. Consequently, considerable efforts have been devoted to enhancing the water flux, antifouling properties, and separation performance of TFC membranes, leading to the development of special TFC−FO membranes. For instance, Han et al. reported the

Received: October 11, 2023
Revised: December 13, 2023
Accepted: December 20, 2023
Published: December 30, 2023



Downloaded from pubs.acs.org/iecred/article-pdf/63/1/566/1502927/ie3c03579.pdf by DOKUZ EYLUL UNIV user on 03 September 2026

ACS Publications
© 2023 American Chemical Society

https://doi.org/10.1021/acs.iecr.3c03579
Ind. Eng. Chem. Res. 2024, 63, 566−578

successful fabrication of a thin-film nanocomposite (TFN) membrane designed for the rejection of monovalent and divalent salts, utilizing amine-containing Cr-based metal−organic framework (MOF) nanoparticles. The resulting membrane, prepared through postmodification of the MOF, exhibited high rejection rates for NaCl, $MgCl_2$, Na_2SO_4, and $MgSO_4$ under low-pressure conditions.[23] In another project from the same research group, a double-skin TFC hollow fiber FO membrane structure was designed by introducing two inner and outer PA layers through a secondary interfacial polymerization (IP) reaction. The results of this study demonstrated promising outcomes for concentration polarization (CP) and fouling mitigation.[24] Similarly, Hakimi et al. reported on the utilization of poly(ethylene glycol) diamine as a novel functional monomer to modify a TFC membrane. The fabricated membrane exhibited a significant increase in water flux and antifouling improvement owing to the smoother and more hydrophilic surface.[25] Additionally, the capability of the TFC membrane to mitigate fouling tendencies has been successfully investigated in a pressure-retarded osmosis (PRO) operation, utilizing wastewater brine as the DS and desalination brine as the FS. It has been demonstrated that the use of antiscalant pretreatment and pH adjustment in the DS yields promising results for fouling mitigation.[26]

Since the PA selective layer, formed by the IP reaction, controls the transport properties of TFC membranes, it is rational to tailor the morphology and chemical properties of the PA layer. Different modification methods have been employed, like incorporating hydrophilic additives, such as nanomaterials, and polymers.[27−29] Recently, attention has been focused on incorporating hydrophilic nature-based polymeric structures within the active layer that have lower toxicity, fewer environmental impacts, and a lower economic cost for membrane fabrication.[30] Among them, biopolymeric nanomaterials, such as cellulose nanocrystals, chitosan, cellulose nanofibers (CNFs), and cyclodextrin, had a significant contribution in fabricating TFN membranes.[31,32]

Cellulose is the most abundant natural "organic" biomaterial on the earth. In this class of materials, CNFs, made up of nanosized cellulose fibrils, can be obtained readily from renewable and sustainable resources like cotton pulp, wheat, and wood.[33] It is a promising material for membrane fabrication/modification because of its eco-friendliness, low health impacts, high mechanical strength, and high surface-to-volume ratio.[34−36] Besides, the abundant hydroxyl groups in CNF structures not only facilitate their further functionalization but also impart exceptional hydrophilicity to them.[37]

Anchoring hydrophilic polymer networks to the membrane surface reduces the foulant adsorption and thus can positively enhance the antifouling properties. This chemical surface modification is usually conducted by UV-induced,[38] physical adsorption,[39] and grafting "from or to" methods.[40] In this regard, incorporating zwitterions in the membrane has been extensively reported as a promising and successful method to mitigate the membrane fouling propensity.[41,42] Zwitterions are neutral monomers possessing an equimolar number of homogeneously distributed positively and negatively charged components on their polymer chains. Therefore, zwitterions can remarkably absorb and bind water molecules via electrostatic interactions. This process creates a steric repulsion effect that significantly prevents foulant attachment to the membrane surface.[43,44] In this work, we used CNF-*g*-PSBMA [PSBMA = poly(sulfobetaine methacrylate)] as an additive to fabricate hydrophilic and antifouling TFN FO membranes. The zwitterionic polymer CNF-*g*-PSBMA was synthesized with the SBMA monomer through grafting from polymerization on CNFs. CNF-*g*-PSBMA was incorporated into the active layer to improve membrane properties. The resulting modified membrane demonstrated a smoother, thinner, and more hydrophilic PA layer compared with the pristine membrane. The performance of the synthesized membranes was evaluated in terms of the water flux, reverse solute flux, and foulant adsorption. To the best of our knowledge, this work is the first study of the utilization of CNF-*g*-PSBMA for fouling control of TFN FO membranes.

2. EXPERIMENTAL SECTION

2.1. Chemicals and Reagents. Poly(ether sulfone) (M_w: 58,000) (PES S6020, Ultrason, BASF Co, Merck, Germany), *N*-methyl-2-pyrrolidone (NMP), and polyethylene glycol 400 (PEG-400) (Merck) were used as the polymeric support, solvent, and pore-forming agent, respectively. Trimesoyl chloride (TMC, 98%, Merck, organic-phase monomer), hexane (98%), and *m*-phenylenediamine (MPD, >99%, Merck, aqueous-phase monomer) were utilized to form the PA layer. CNF-*g*-PSBMA was synthesized using CNFs (Sigma-Aldrich), 3-methacryloxypropyltrimethoxysilane (MPS, silane coupling agent), SBMA (Sigma-Aldrich), and azobis-(isobutyronitrile) (AIBN, initiator). The FO tests were conducted using deionized (DI) water and various concentrations of NaCl (1, 2, and 3 M) (Iran Mineral Sal Co) as the FS and DS, respectively. Two model foulants, bovine serum albumin (BSA) and sodium alginate (SA), were used in the fouling test cycles.

2.2. Synthesis of Vinyl-Modified CNFs and CNF-*g*-PSBMA Polymer. Preparation of the macroinitiator was conducted as follows: in brief, 1 g of CNFs was dispersed in the mixture of ethanol/water with a ratio of (4/1) (30 mL). The mixture was ultrasonicated to yield a homogeneous solution. The reaction media was then treated with 2 mL of 25 wt % ammonia aqueous solution to adjust the pH to 10. Subsequently, 2−3 mL of MPS silane coupling agent was added dropwise to the mixture.[45] The solution was stirred overnight at 75 °C. Then, the precipitate (denoted as CNF-MPS) was centrifuged and washed with toluene several times. The final product was dried in the oven overnight.

To prepare CNF-*g*-PSBMA, 0.1 g of synthesized CNF-MPS was sonicated for 15 min in 10 mL of dimethyl sulfoxide. Then, the flask was filled with 0.4 g of SBMA monomer, and the reaction was allowed for 2 h to achieve a homogeneous prepolymerization solution. Next, 0.08 g of AIBN, serving as a free-radical polymerization initiator, was added to the reaction media. This step was followed by purging with nitrogen (N_2) for 15 min. The polymerization process was then carried out at 80 °C for a duration of 2 h. To eliminate unreacted monomers and nongrafted free polymers, CNF-*g*-PSBMA was centrifuged and rinsed three times with DI water. Finally, the product was freeze-dried and kept for further characterization.

2.3. Preparation of the FO Support Layer and TFC/TFN Membranes. The PES substrate was fabricated by nonsolvent-induced phase inversion (NIPS). PES has excellent chemical and thermal stability for PA TFC synthesis.[46] PES flakes (15 wt %), NMP (20 wt %), and PEG (65 wt %) were mixed and stirred until the polymer solution became homogeneous and transparent. After degassing for 12 h, the polymer solution was cast onto a glass plate using a 100 μm

Downloaded from pubs.acs.org/iecred/article-pdf/63/1/566/1502927/ie3c03579.pdf by DOKUZ EYLUL UNIV user on 03 September 2026

https://doi.org/10.1021/acs.iecr.3c03579
Ind. Eng. Chem. Res. 2024, 63, 566−578

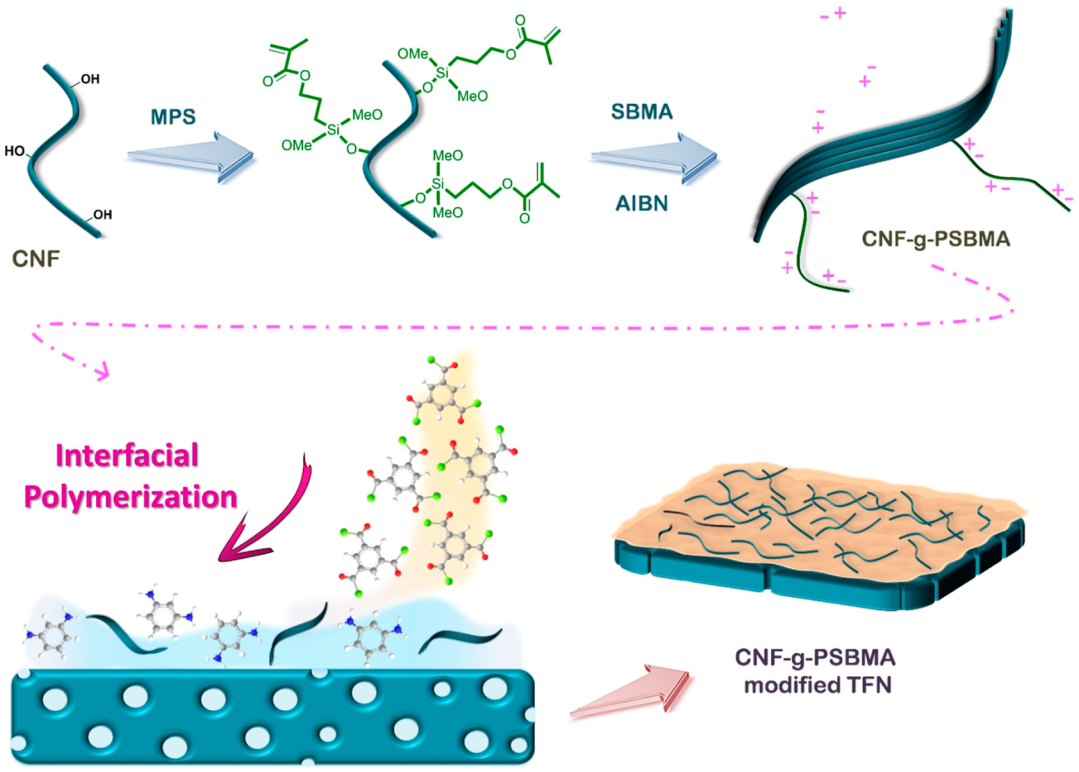


Figure 1. Schematic representation of synthesis of CNF-*g*-PSBMA, and fabrication of a modified TFN membrane. The synthesized polymer was mixed with MPD solution prior to IP.

thick casting knife and immediately immersed in a DI water coagulation bath at ambient temperature. Subsequently, the solution experienced the phase-inversion process. The PES substrate was washed with DI water and stored in DI water for further use.

Membrane fabrication conditions, encompassing the TMC/MPD concentration, curing temperature, and reaction time, were preliminarily optimized. CNF-*g*-PSBMA-modified TFN membranes were prepared by an IP reaction. A schematic illustration of the preparation procedure is provided in Figure 1. An aqueous solution of MPD (2 wt %) and CNF-*g*-PSBMA with different concentrations (50, 100, and 200 ppm) was sonicated for 15 min to obtain a uniform suspension. Then, the resulting mixture was poured on the top surface of the PES substrate and left for 2 min. After removing excess MPD drops with a rubber roller, the membrane TMC solution was poured on top of the support (0.1 wt %) and left for 1.5 min to conduct the IP reaction between MPD, CNF-*g*-PSBMA, and TMC. The excess solution was drained off, and the treated membrane was then subjected to post-treatment in an oven at 60 °C for 1 min to stabilize the membrane structure. Finally, the CNF-*g*-PSBMA-modified membrane was thoroughly rinsed and kept in DI water for subsequent experiments.

The resultant TFN membranes were labeled based on the concentration of CNF-*g*-PSBMA in aqueous solution as TFN-50, TFN-100, and TFN-200. A pristine TFC membrane was also fabricated without incorporating CNF-*g*-PSBMA, which served as a blank sample for comparison.

2.4. Characterization of Synthesized Materials and Membranes. The chemical composition of synthesized CNFs and CNF-*g*-PSBMA was investigated using Fourier transform infrared (FTIR) spectroscopy (Equinox-55 FTIR) at room temperature in the range of 600−4000 cm^{-1}. The thermal behavior of the prepared samples was studied using thermogravimetric analysis (TGA) by a Q5000IR (TA Instruments, USA). The samples were heated under an N_2 atmosphere at a rate of 10 °C/min. X-ray diffraction (XRD) (PW1730, Philips) and scanning electron microscopy (SEM, Tescan, VEGA) were conducted to study the crystalline structure and size of CNF-*g*-PSBMA, respectively.

Furthermore, attenuated total reflectance (ATR)-FTIR spectroscopy (Thermo Nicolet Nexus 670, USA) was used to examine the functional groups on the surface of the synthesized membranes over a 600−4000 cm^{-1} wavenumber range.

Atomic force microscopy (AFM) was used to examine the surface topography of the TFN membranes (ENTEGRA AFMNT-MDT). Field-emission scanning electron microscopy (FESEM) was used to analyze the surface morphology of the membranes (Zeiss Sigma 300 VP and JEOL 6301F). Membranes were coated with carbon before the FESEM test. In addition, transmission electron microscopy (TEM, Philips/FEI Morgagni 268, The Netherlands) was utilized to study the cross-sectional features of the PA active layer. Elemental mapping analysis was performed using the energy-dispersive X-ray spectroscopy (EDX, Bruker) acquisition system.

The surface hydrophilicity of the manufactured membranes was studied by measuring the static water contact angle (WCA) data using a Dataphysics, OCA 15Plus instrument. The zeta potential was used to evaluate the membrane surface charge. This analysis was done using a SurPASS 3 electrokinetic surface potential analyzer in a pH range of 3−9 (Anton Paar, Graz, Austria). Characterization tests were repeated three times for each sample, and the average values were reported.

2.5. Investigation of TFC/TFN Membrane Performance. Solvent permeance and solute permeability are intrinsic

https://doi.org/10.1021/acs.iecr.3c03579
Ind. Eng. Chem. Res. 2024, 63, 566−578

Downloaded from pubs.acs.org/iecred/article-pdf/63/1/566/1502927/ie3c03579.pdf by DOKUZ EYLUL UNIV user on 03 September 2026

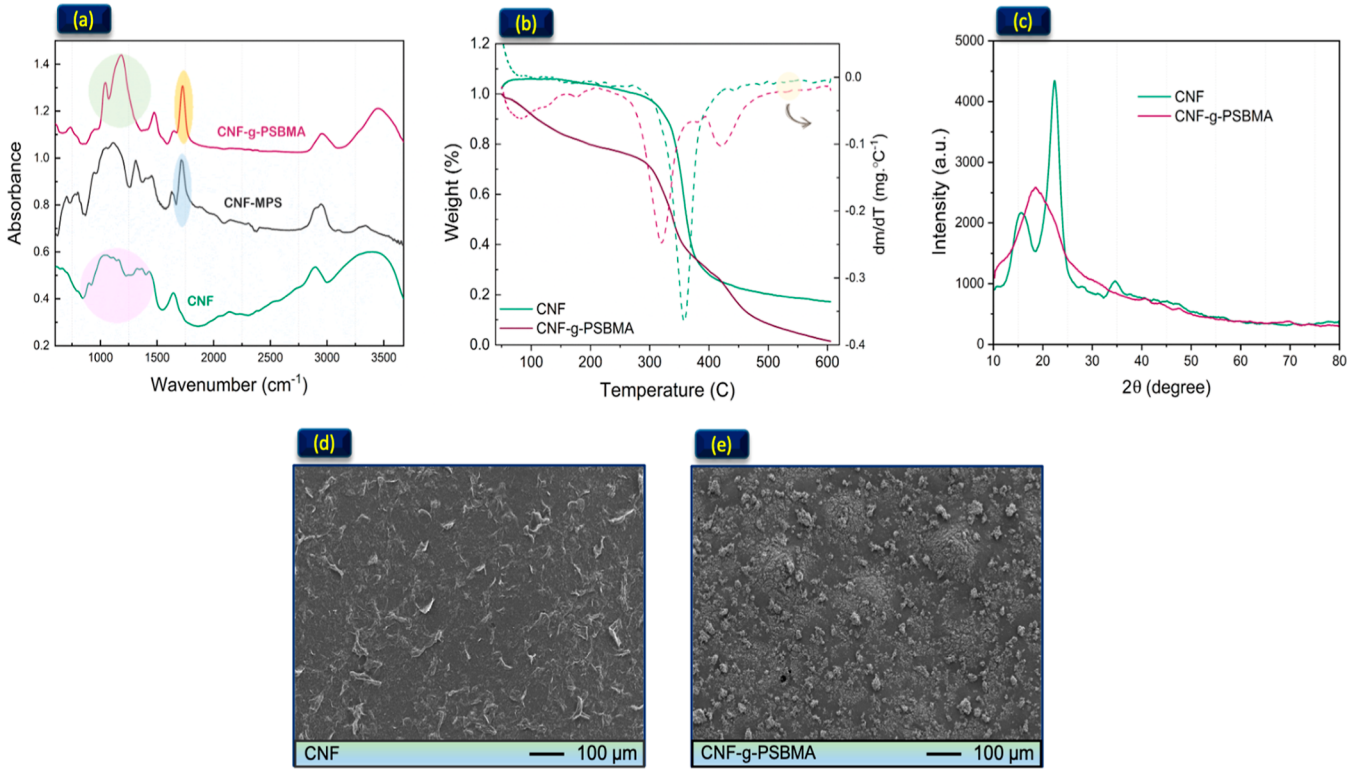


Figure 2. Characterization of CNFs and CNF-*g*-PSBMA. (a) FTIR spectra, (b) TGA curves, (c) XRD patterns, and (d,e) SEM images, indicating the successful modification of CNFs with PSBMA.

transport characteristics. NaCl and water were utilized as the solute and solvent in this investigation, respectively. Under a hydraulic pressure of 5.0 bar, a stirred lab-scale RO filtration system with an effective membrane area of 3.14 cm^2 was utilized to evaluate the solute permeability (B), pure water permeance (A), as well as solute rejection (R). The data that have been reported are the test average results. It should be noted that the RO filtration system was initially run for 20 min to get a stable flux before being subjected to an additional hour of testing. The following equations were used to calculate the intrinsic transport parameters:

The coefficient A (commonly abbreviated as LMHB) was determined as follows

$$A = \frac{J_w}{\Delta P} \tag{1}$$

$$J_w = \frac{\Delta V}{A_m \Delta t} \tag{2}$$

where A is the pure water permeance coefficient (L m^{2-} h^{-1} bar^{-1}, commonly abbreviated as LMHB), ΔP (bar) is the transmembrane pressure, and J_w is the permeate flux. J_w is calculated by dividing the volume (ΔV) of permeated water (L) through the membrane with an active surface area A (m^2) during the test duration t (h).

For calculating the solute permeability (B, LMH) and solute rejection (R %), 1000 mg of L^{-1} NaCl solution was used as the FS. The following equations are used to calculate B and R

$$R = \left(1 - \frac{C_p}{C_f}\right) \times 100 \tag{3}$$

$$\frac{1 - R}{R} = \frac{B}{A(\Delta P - \Delta \pi)} \tag{4}$$

where C_p and C_f are the concentrations of solute in the permeate and FS, respectively, and $\Delta\pi$ is the osmotic pressure difference.

To get a deeper insight into membrane performance, we employed a lab-scale FO setup featuring a membrane cell with an effective surface area of 4.9 cm^2. The system was operated at a 100 mL/min flow rate (cross-flow velocity of 20.4 cm/s) at 25 °C. 1 M NaCl solution and DI water were used as the DS and FS, respectively. Two variable-speed pumps were used to circulate DI and NaCl solutions counter-currently through the cell channels. Before the 1 h performance measurement, the FO and PRO operations were run for 10 min to establish a constant water flux before capturing the final values. In this experiment, both the FO mode, in which the active layer faces the FS, and the PRO mode, in which the active layer faces the DS, were tested to evaluate all polymer-modified TFNs and control-TFC. Two sets of data were recorded, depending on the operational mode. Each test was conducted three times for 1 h, with the average results being reported to reduce potential experimental mistakes and produce more reliable results.

The water flux (J_w, LMH) and the reverse salt flux (J_s, gMH) were obtained by recording the change in the FS volume (V_t, L) and its salt concentration (C_t, g/L) throughout the testing time (t, h), respectively. Moreover, using a portable conductivity meter (WTW GmbH, Germany), the feed concentration was measured.

$$J_w = \frac{\Delta V}{A_m \Delta t} \tag{5}$$

https://doi.org/10.1021/acs.iecr.3c03579
Ind. Eng. Chem. Res. 2024, 63, 566−578

Downloaded from pubs.acs.org/iecred/article-pdf/63/1/566/1502927/ie3c03579.pdf by DOKUZ EYLUL UNIV user on 03 September 2026

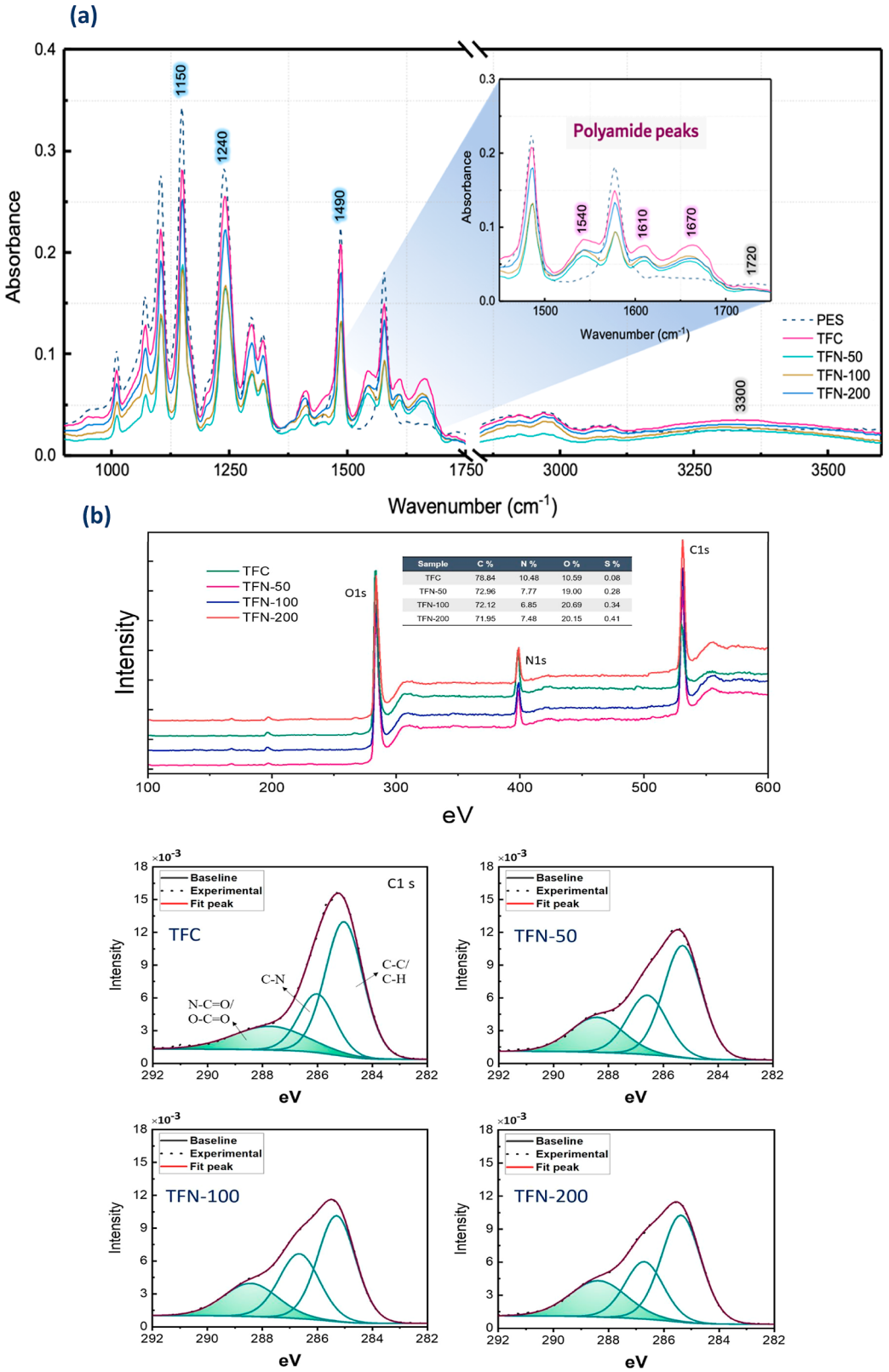


Figure 3. (a) Absorbance spectrum of TFC/TFN membranes obtained by ATR-FTIR analysis. (b) XPS high-resolution deconvoluted carbon peaks of TFC and TFN membranes.

$$J_S = \frac{\Delta(C_t V_t)}{A_m \Delta t} \quad (6)$$

To evaluate the antifouling propensity of FO membranes, protein and polysaccharides were frequently utilized as foulants. Herein, the model foulants, BSA and SA (containing 0.5 mM $CaCl_2$) were dissolved in DI water (total concentration of 600 ppm, 25 °C) and used as the FS. The DS consisted of a 1 M NaCl solution.

https://doi.org/10.1021/acs.iecr.3c03579
Ind. Eng. Chem. Res. 2024, 63, 566−578

Downloaded from pubs.acs.org/iecred/article-pdf/63/1/566/1502927/ie3c03579.pdf by DOKUZ EYLUL UNIV user on 03 September 2026

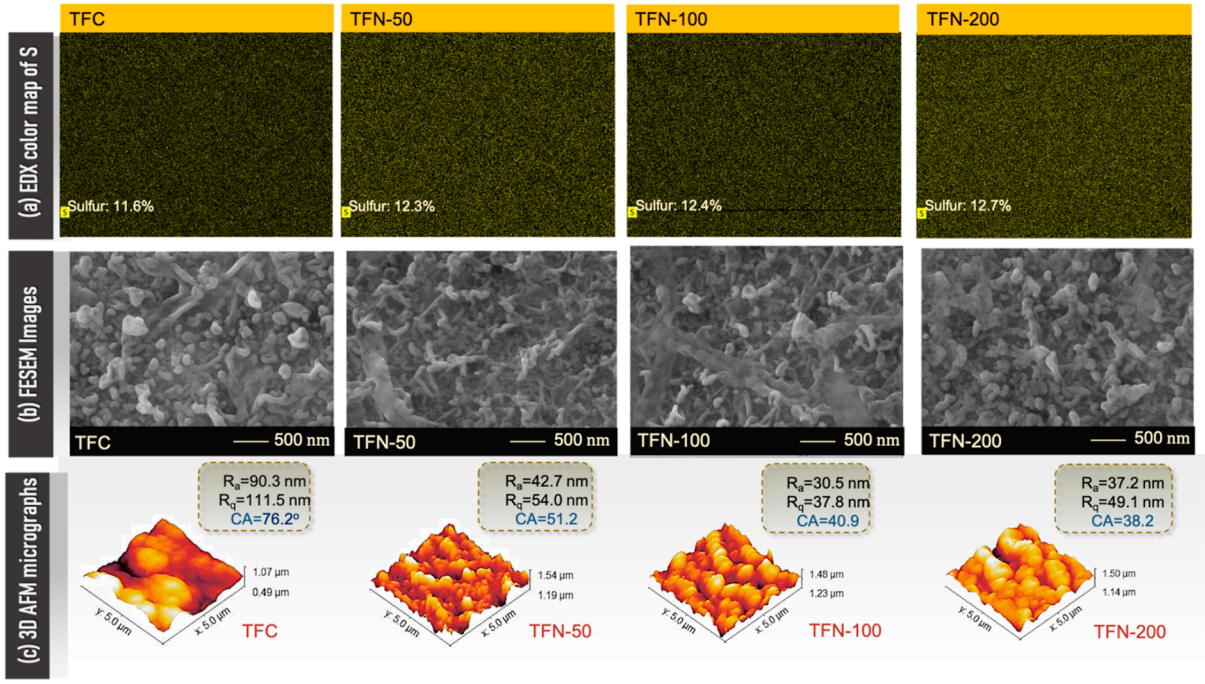


Figure 4. (a) EDX color maps of S, (b) FESEM images, and (c) 3D AFM micrographs and contact angles of synthesized membranes, indicating improved hydrophilicity of TFC/TFN membranes.

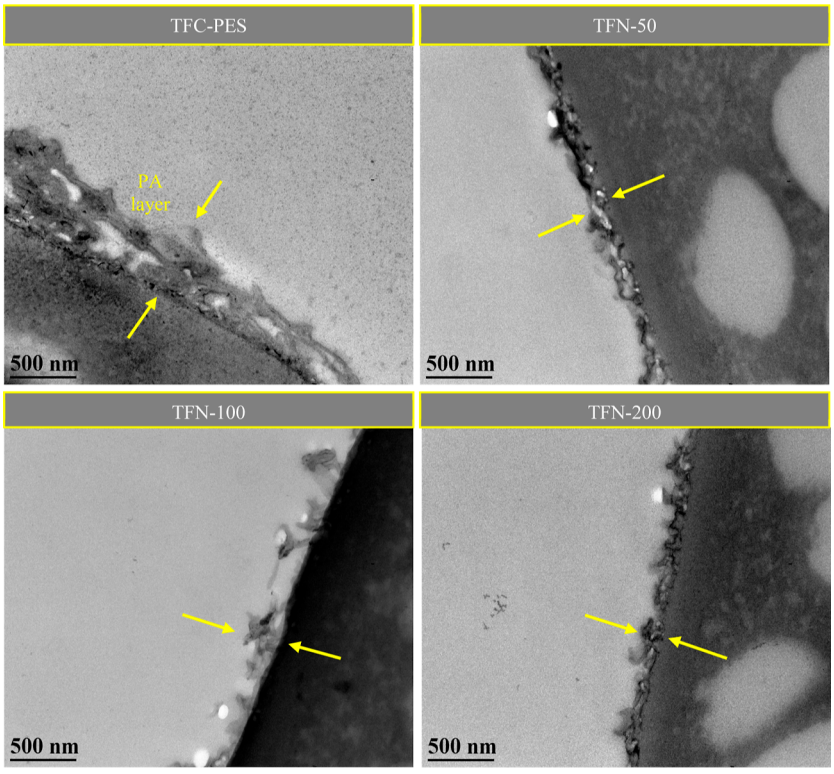


Figure 5. Cross-sectional TEM images of membranes. The internal voids inside the PA were formed during IP due to the heat release of the MPD/TMC reaction.

The same FO cross-flow system at a flow rate of 70 mL/min (cross-flow velocity around 14.3 cm/s) was used for the antifouling investigations. In the first step, a pure water flux test was conducted for 15 min, and the stable water flux (J_0) was recorded. Then, the FS was replaced with a model fouling solution at a concentration of 600 ppm. The change in the membrane flux was recorded at intervals of 10 min. After that, the contaminated membrane samples were washed for 1 h by the circulation of DI water at a higher flow velocity of 20.4 cm/s in both channels of the membrane cell. To quantify the fouling behavior, the flux decline rate (R_t) and the flux recovery ratio (FRR) were calculated as follows

https://doi.org/10.1021/acs.iecr.3c03579
Ind. Eng. Chem. Res. 2024, 63, 566−578

Downloaded from pubs.acs.org/iecred/article-pdf/63/1/566/1502927/ie3c03579.pdf by DOKUZ EYLUL UNIV user on 03 September 2026

$$\mathrm{FRR} = \left(\frac{J_R}{J_0}\right) \times 100 \tag{7}$$

$$R_t = \frac{J_0 - J_S}{J_0} \tag{8}$$

where J_0 is the initial flux, J_s is the steady water flux after fouling, and J_R is the recovered flux after washing.

3. RESULTS AND DISCUSSION

3.1. Characterization of CNF-*g*-PSBMA. The FTIR spectra of CNF, CNF−MPS, and CNF-*g*-PSBMA are shown in Figure 2a. All samples revealed a broad band at 3200−3500 cm^{-1} and a band between 2890 and 2960 cm^{-1}, related to O−H and c-H stretching vibrations, respectively. In the spectrum of CNFs, the characteristic peaks of cellulosic β-glycosidic linkages (C−O−C) and pyranose ring (C−O) were observed at 892 and 1058 cm^{-1}, respectively.[47] The spectral band observed in CNFs at around 1640 cm^{-1} was due to the bending of adsorbed water. Despite drying the sample before FTIR analysis, the complete removal of water from CNF was difficult because of the strong cellulose−water interactions.[48] Finally, the CH_2 wagging motion and scissoring were observed at 1317 and 1430 cm^{-1}, respectively.[49]

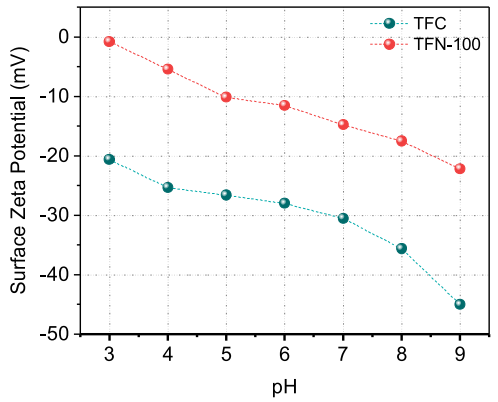


Figure 6. Surface zeta potential of TFC and TFN-100 membranes over pH 3−9.

After MPS modification, the O−H peak intensity was noticeably reduced in the 3200−3500 cm^{-1} region, and a new peak appeared at 1714 cm^{-1}, corresponding to C═O stretching in CNF-MPS.[50] This observation demonstrates the successful modification of CNF with MPS. In the CNF-*g*-PSBMA spectrum, the characteristic peaks of the S═O bond in PSBMA could be found at 1041 cm^{-1} (symmetric) and 1160 cm^{-1} (asymmetric).[51] The shoulder peak at 1643 cm^{-1} was assigned to the stretching vibration of the C−N^+ bond. The results further confirm the successful synthesis of CNF-*g*-PSBMA.

Figure 2b shows the weight loss of prepared samples as a function of temperature obtained by TGA. The degradation of CNFs involved one major degradation stage, typical for the crystalline structure of cellulosic materials. The TGA curve of CNF-*g*-PSBMA demonstrated an initial weight loss of 27% in a low-temperature range below 200 °C, attributed to the loosely bound surface water and solvent in the polymer structure. Approximately 75% of CNF-*g*-PSBMA degraded between 270 and 600 °C, with hemicelluloses undergoing thermal depolymerization and glycosidic linkages breaking around 300 °C.[52] Subsequently, the thermal degradation of PSBMA polymeric chains and pendant groups, including quaternary ammonium and sulfonate groups, occurred at 400 °C.[53] A degradation shift was observed in thermogram of CNF-*g*-PSBMA compared to the original CNF. The substantial weight loss of the final polymer (around 40%) initiated at approximately 270 °C, indicating a shift of about 30 °C compared to CNFs. This shift is likely attributable to the catalytic effect of sulfonic acid.[54]

XRD patterns of CNFs and CNF-*g*-PSBMA are provided in Figure 2c to study their crystalline structure. CNF crystalline structure was clearly represented by two well-defined diffraction peaks in the vicinity of 2θ = 22.5 and 15.3°. These signals were attributed to the interplanar distances of cellulose 1_α and 1_β phases, respectively.[55] In the XRD pattern of CNF-*g*-PSBMA, a decrease in the crystallinity pattern confirms the successful modification by the amorphous polymeric group.[56]

To study the morphology and size of CNFs before and after PSBMA grafting, SEM micrographs were taken. Figure 2d displays the CNF morphology before grafting, and Figure 2e shows the morphology after grafting. According to the images, CNFs were observed as fibers arranged in a stack, with an

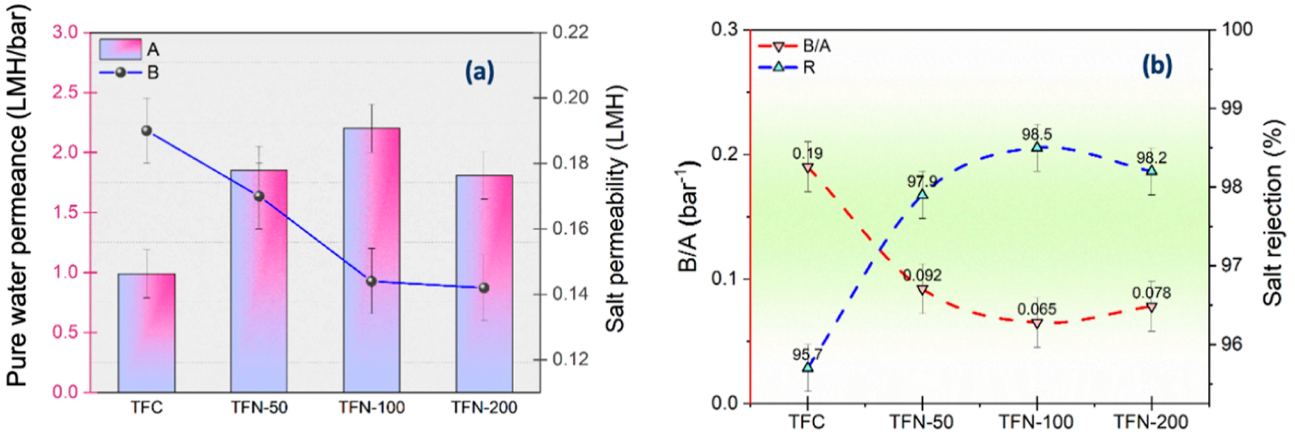


Figure 7. Intrinsic transport properties of different membranes: (a) pure water permeance and salt permeability and (b) selectivity ratio and salt rejection.

Downloaded from pubs.acs.org/iecred/article-pdf/63/1/566/1502927/ie3c03579.pdf by DOKUZ EYLUL UNIV user on 03 September 2026

https://doi.org/10.1021/acs.iecr.3c03579
Ind. Eng. Chem. Res. 2024, 63, 566−578

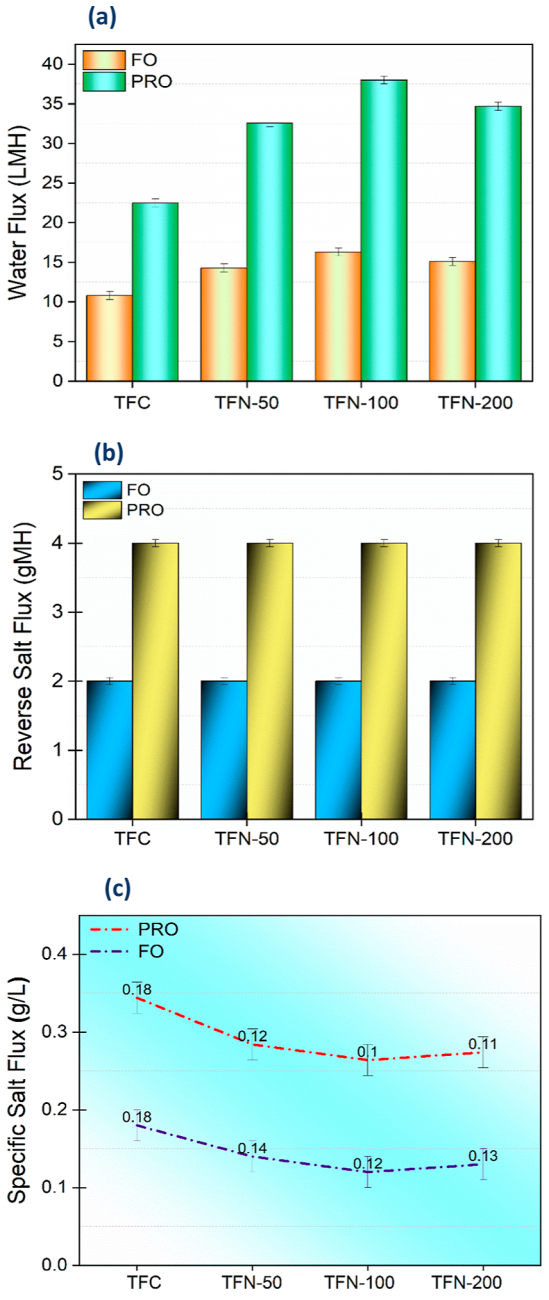


Figure 8. Membrane performance: (a) water flux, (b) reverse salt flux, and (c) specific salt flux of membranes in the FO and PRO modes.

estimated diameter of 8.5 μm and a length of 100 μm. The explanation for this observation lies in the fact that the homogeneity and morphology of nanofibers could be affected by chemo-mechanical treatment.[47] Lignocellulosic materials contain various binding compounds such as hemicellulose, lignin, and pectin, which make it challenging (requires intensive mechanical methods such as high-intensity ultrasonic treatment and grinding) to isolate the cellulosic chain and to obtain defibrillated cellulose. Additionally, the NFs might join together through hydrogen bonds to create microfibers.[57,58] Figure 2e reveals that PSBMA grafting led to the appearance of irregular spheres with sizes ranging from 10 to 32 μm and a distinct increase in the coarseness of CNFs. The PSBMA grafting is believed to prevent CNF agglomeration, resulting in a PA layer with more efficient antifouling properties.

3.2. Characterization of the Synthesized Membranes.

Figure 3a shows the ATR-FTIR spectra of the PES substrate and prepared TFC/TFN membranes. The peaks related to the PES support appeared at 1150, 1240, and 1490 cm^{-1}, which were assigned to the symmetric sulfone groups, aryl-O-aryl C−O stretching vibrations, and aromatic ring stretching vibrations, respectively. The PA layer was responsible for the three distinct peaks in the spectra of the TFC and TFN membranes at 1670 cm^{-1} (C═O stretching vibrations of amide I), 1610 cm^{-1} (stretching vibrations of the C═C aromatic amide ring), and 1540 cm^{-1} (N−H bending of amide II and stretching vibrations of C−N). These peaks confirm the successful formation of a selective PA layer over the PES support.[59] In the spectra of all CNF-*g*-PSBMA-modified TFN membranes, the PA peak intensity was lower than that of the pristine TFC. This decrease in intensity might be due to the reduced formation of amide linkages in the PA layer. The presence of CNF-*g*-PSBMA in the aqueous phase reduced the amine monomer diffusion during IP to the reaction zone, resulting in decreased PA production. As the micrometer detection depth of the ATR-FTIR technique was much higher than the nanometer-scale thickness of the PA layer, the absorption peaks of the PES substrate were also observed in all of the TFC/TFN spectra.

Figure 3b displays both the general survey spectral and high-resolution C 1s peaks of TFC, TFN-50, TFN-100, and TFN-200. The general survey spectrum indicates the existence of carbon (at 285 eV), nitrogen (at 400.5 eV), oxygen (at 532 eV), and sulfur (at 165 eV) in the fabricated membranes. By increasing the concentration of CNF-*g*-PSBMA to 200 ppm, the content of sulfur increased, indicating a higher loading of CNF-*g*-PSBMA into the polyimide matrix.

The inset table in the image lists the peak area ratios for carbon chemical bonds. The high-resolution C 1s spectra for TFC and TFN membranes were deconvoluted, yielding the following peaks: C−C/C−H at 285 eV, − CN− at 286.5 eV, and N−C═O/O−C═O at 288.2 eV. The increase of O═C═O functional groups in membranes is attributed to the presence of CNF-*g*-PSBMA. While CNF-*g*-PSBMA has no groups with the O═C═O group in its structure, it can influence the PA composition, leading to an increased abundance of the O−C═O moieties. Presence of CNF-*g*-PSBMA in the polymerization medium reduced the reactivity between MPD and TMC during the IP. The reduced reaction resulted in a higher concentration of unreacted TMC monomers within the membrane matrix. Following hydrolysis, these unreacted TMC monomers were converted to carboxylic groups.

In addition, EDX elemental mapping proved that the CNF-*g*-PSBMA polymer was successfully incorporated within the TFN membranes (Figure 4a). The analysis of this figure shows that the sulfur content increased from 11.6% in TFC to 12.7% in TFN-200. This increase was due to more loading of CNF-*g*-PSBMA polymer in the PA layer.

Figure 4b shows the top surface SEM images of the synthesized membranes. The pristine TFC and CNF-*g*-PSBMA-modified TFN membranes had a ridge-and-valley structure typical for the PA active layer synthesized via the IP reaction.[60] However, the top surface of the CNF-*g*-PSBMA-modified TFN membranes had smaller surface features. This observation was further confirmed by the 3D AFM images, where the CNF-*g*-PSBMA-modified TFN membranes had a smoother surface with fewer ridges and valleys. According to

Downloaded from pubs.acs.org/iecred/article-pdf/63/1/566/1502927/ie3c03579.pdf by DOKUZ EYLUL UNIV user on 03 September 2026

https://doi.org/10.1021/acs.iecr.3c03579
Ind. Eng. Chem. Res. 2024, 63, 566−578

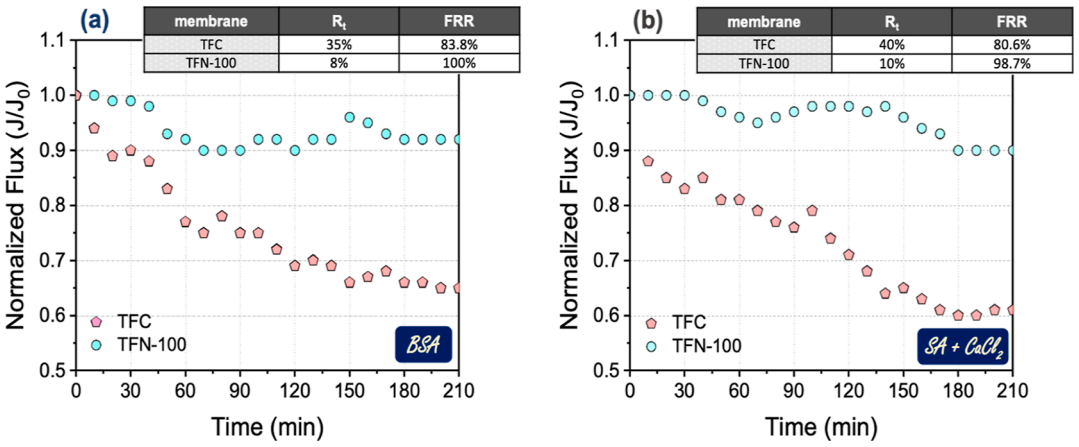


Figure 9. Fouling behavior and flux recovery rate of TFC and modified membranes for (a) BSA and (b) SA foulants (foulants as FS with 600 ppm concentration and 1 M NaCl as DS).

Table 1. Comparison between the Performance of Synthesized TFN-100 and Those from Other Literature Sources

	FO performance			RO performance			
membrane	J_w (LMH)	J_s (gMH)	J_s/J_w (g/L)	A (LMH/bar)	B (LMH)	B/A (1/bar)	reference
TMC/MPD-PEI	15	5.2	0.16	1.51	0.31	0.21	42
CATCP	12.1	3	0.25				78
PDA/MOF/TFN	16.5	3.3	0.2	2.12	0.88	0.42	79
TFN/PDA-CNT	7.9	1.7	0.22				80
TFN-100	**16.3**	**2**	**0.12**	**2.2**	**0.14**	**0.065**	**this work**

AFM images (Figure 4c), the R_a values decreased substantially from 90.3 nm for pristine TFC to the minimum amount of 30.5 nm for TNF-100. A smooth PA layer is expected to improve the membranes' antifouling properties by reducing hot spots (valleys on the membrane surface) for foulants' deposition.[61,62]

The observations above could be explained by the fact that CNF-*g*-PSBMA regulated IP by controlling the MPD diffusion rate from the aqueous phase to the organic phase, where the polymerization reaction took place. The slower the MPD migration, the smoother and more uniform the membrane surface becomes.[63] Upon the addition of hydrophilic CNF-*g*-PSBMA, the hydrogen bonds between CNF-*g*-PSBMA and MPD mitigated the diffusion of MPD to the reaction zone. This slowed down the reaction kinetics and thus reduced the roughness of modified membranes compared to the unmodified TFC membrane.[64]

The effect of CNF-*g*-PSBMA incorporation on the TFN surface hydrophilicity was studied using WCA measurements (Figure 4c). By increasing the concentration of CNF-*g*-PSBMA, the hydrophilicity of membranes increased, where the WCA decreased from 51° for TFN-50 to 38.2° for TFN-200. The higher hydrophilicity of TFN membranes is due to incorporation of the CNF-*g*-PSBMA polymer with abundant hydrophilic hydroxyl, sulfonic acid, and oxygen-containing groups into the PA active layer.[65] The strong hydrogen bonding between water molecules and these functional groups generates a dense hydration layer on the support layer, preventing contaminants from attaching to the membrane surface.

The cross-sectional TEM images of the prepared membranes are provided in Figure 5. As can be seen, the PA active layer was uniformly formed on the surface of the PES support. The PA layer thickness was notably decreased from 500 nm for the pristine TFC to an average of 200 nm for the modified TFN membranes. Lower PA thickness enhances the mass transfer of the CNF-*g*-PSBMA-modified membranes by reducing the resistance to water permeation. As mentioned earlier, the CNF-*g*-PSBMA incorporation reduced the rate of MPD diffusion during the IP reaction. Less polymerization on the organic side resulted in reduced polymer growth over the PA surface and a lower PA layer thickness, consistent with the lower intensity of PA characteristic peaks in the FTIR spectra (see Figure 3).[66]

Figure 6 shows the streaming zeta potential profiles of the TFC and TFN-100 membranes as a function of pH. The PA active layer of the TFC membrane contained carboxylic groups, resulting from the hydrolysis of the COCl groups of TMC monomers. Hence, due to the deprotonation of carboxylic groups, the surface became more negatively charged when the pH increased. The membrane zeta potentials for CNF-*g*-PSBMA-modified membranes were more positive than that of the TFC membrane. This could be justified by the presence of neutrally charged zwitterionic PSBMA in the synthesized polymer, whose cationic quaternary amine groups neutralized the carboxyl groups on the membrane surface. However, due to the negative charge of TFNs, it seems that the sulfonic group still controlled and dictated the overall charge of TFN-100.[67] Zwitterionic polymer modification is a viable approach to exploiting the electrostatic repulsion toward different foulants by minimizing the charge-induced membrane fouling, primarily when divalent ions are present in the wastewater. The possibility of negatively charged carboxyl interaction with cations such as calcium ions can form a densely packed fouling layer, reducing the water flux significantly.[68,69]

3.3. Effect of CNF-*g*-PSBMA on Membrane Performance and Antifouling Properties. The pure water

https://doi.org/10.1021/acs.iecr.3c03579
Ind. Eng. Chem. Res. 2024, 63, 566−578

Downloaded from pubs.acs.org/iecred/article-pdf/63/1/566/1502927/ie3c03579.pdf by DOKUZ EYLUL UNIV user on 03 September 2026

permeance (A), solute permeability (B), and solute rejection (R) were evaluated by a series of RO filtrations. Figure 7 shows that the CNF-*g*-PSBMA modification enhanced the pure water permeance from 0.99 LMH/bar for TFC to 2.2 LMH/bar for TFN-100. The solute rejection (R) improved for all modified membranes compared with the TFC membrane, with maximum and minimum values of 98.5 and 97.9% for TFN-100 and TFN-50, respectively. The solute permeability exhibited a downward trend with an increase in the CNF-*g*-PSBMA content: TFN-200 < TFN-100 < TFN-50 < TFC. The solute permeability reached a minimum value of 0.142 LMH for TFN-200, almost 1.4 times lower than the bare TFC. The intrinsic selectivity ratio (B/A) is a determining parameter for TFC-FO membrane selectivity. A lower B/A value is desirable in an FO process, indicating greater membrane selectivity. Figure 7b reveals that the addition of CNF-*g*-PSBMA improved the selectivity properties of the TFN membranes. TFN-100 had the lowest B/A ratio (0.065 bar^{-1}) and can be considered as the optimum membrane in terms of separation performance.

Likely explanations for the increased pure water permeance by adding CNF-*g*-PSBMA include (i) the reduction in PA layer thickness, as shown in TEM images, which reduces the mass-transfer resistance; (ii) the generation of new selective nanochannels, facilitating the passage of water molecules while hindering salt penetration,[70,71] and (iii) enhancement in membrane hydrophilicity, as discussed in WCA analysis, leading to more hydrogen bonds with water molecules.[72]

The performance of the prepared TFC FO membranes in terms of water flux, reverse salt flux, and specific salt flux is illustrated in Figure 8a. All the CNF-*g*-PSBMA-modified membranes demonstrated a higher water flux in both FO and PRO modes than the pristine TFC membrane. TFN-100 and pristine TFC had water fluxes of 16.3 and 10.8 LMH in FO mode and 38.0 and 22.5 LMH in PRO mode, respectively. However, a further increase in the CNF-*g*-PSBMA concentration up to 200 ppm resulted in a slight decrease in J_w (compared to TFN-100) in both filtration modes. These observations indicate that additional loading of CNF-*g*-PSBMA may result in polymer agglomeration. A lower dispersion reduces the contribution of the CNF-*g*-PSBMA polymer in the interphase (IP). Consequently, the PA layer is formed with fewer functional materials (CNF-*g*-PSBMA) compared to TFN-100. The reverse salt flux of prepared membranes in Figure 8b implies that the proposed membrane modification improved the water flux without sacrificing salt rejection. In other words, the modified membranes had the same reverse salt flux as the unmodified one in both FO and PRO modes (2 and 4 gMH, respectively).

Water flux and reverse salt flux values of all membranes in PRO mode were higher than those in the FO mode. The internal CP (ICP) effect is more severe in the FO mode because of the presence of NaCl ions in the porous structure of membranes. Therefore, ICP in FO mode reduces the effective driving force for the diffusion of water molecules to the DS.[73] More salt flux in the PRO mode can be explained by the higher concentration of salt ions at the PA surface. In contrast, in the FO mode, the salt concentration is reduced by the diffused water molecules to the support layer of TFC (dilutive ICP).

The specific salt flux, which is defined as the reverse salt flux/water flux, is a crucial factor in evaluating the performance of FO membranes. A smaller specific salt flux is more favorable, showing a lower amount of salt passing through the membrane for each unit volume of permeated water.[74] TFN-100, with the lowest specific salt flux in both filtration modes, exhibited the best selectivity among the synthesized membranes.

Membrane fouling is the most crucial obstacle to the practical application of the FO process. It results from the attachment of biological, organic, inorganic, and colloidal foulants onto the membrane surface and/or within the membrane pores, significantly reducing the membrane longevity as well as the flux and quality of water and, subsequently, increasing the operating costs.

The fouling behavior of the CNF-*g*-PSBMA-based TFN and pristine TFC membranes during the filtration of two model fouling agents, namely, BSA and SA, was investigated. 600 ppm aqueous solutions of BSA and SA + $CaCl_2$ were used as FSs. Figure 9 shows that the water flux of both modified and unmodified membranes had a downward trend during the filtration of both foulants. However, the TFN-100 membrane experienced a more gradual decrease in water flux, reaching a plateau after 60 min of testing, and this trend persisted until the end of the fouling test. In contrast, the pristine TFC membrane exhibited a severe decrease in water flux during the test. In this case, the steady state was reached after approximately 180 min and persisted for the rest of the test. The attainment of the steady state signifies the stabilization of the membrane's performance, showcasing its capacity to sustain a consistent water flux under experimental conditions. This observation highlights the superior potential of TFN-100 compared with TFC in maintaining a stable water flux against fouling.

In the BSA filtration test (Figure 9a), the percentage of flux decline stood at 8% for TFN-100, while for pristine TFC, the flux declined significantly to 35% of the initial flux. A similar trend was also noticed for the SA + $CaCl_2$ fouling agent, with a flux decline of 10% for TFN-100, which was roughly four times lower than that of pristine TFC (~40%). Moreover, comparing the results of two fouling tests showed that the bridging effect of Ca^{2+} ions resulted in a more flux decline during SA solution filtration than BSA for both membranes. Particularly, divalent ions such as Ca^{2+} are expected to form positively charged bridges between negatively charged SA, creating calcium alginate, a gelatinous material that exacerbates the fouling tendency. Additionally, Ca^{2+} makes a bridge between SA foulants and the COOH functional groups of the membrane surface, intensifying membrane fouling.

The flux decline rate (R_t) and the FRR are two important parameters for evaluating the resistance of membranes against fouling. Membranes with a lower R_t and a higher FRR are less prone to fouling.[75] The FRR of the pristine TFC membrane was around 84 and 81% for BSA and SA pollutants, respectively. The incorporation of CNF-*g*-PSBMA increased the FRR to 100 and 98.7%, respectively, suggesting that our modification method improved the antifouling properties of the membranes.

Generally, fouling is governed by the surface hydrophilicity, surface chemistry, and surface roughness of membranes. The enhanced hydrophilicity of the CNF-*g*-PSBMA-modified membrane positively affected its antifouling properties. The higher hydrophilicity of the TFNs decreased the unfavorable hydrophobic/hydrophobic interactions between the fouling agents and the membrane surface by creating a stable hydration layer on the membrane surface. On the contrary, the unmodified TFC was likely readily covered by BSA and SA due to the hydrophobic−hydrophobic interactions between

Downloaded from pubs.acs.org/iecred/article-pdf/63/1/566/1502927/ie3c03579.pdf by DOKUZ EYLUL UNIV user on 03 September 2026

https://doi.org/10.1021/acs.iecr.3c03579
Ind. Eng. Chem. Res. 2024, 63, 566−578

the conjugated benzene rings of the PA active layer and foulants.[76] More importantly, a rougher surface accelerated the fouling tendency, as it provided more hot spots for foulant adsorption. Hence, the smoother surface of TFNs, as evidenced by AFM analysis, could account for its great antifouling properties. The modification of the PA layer with CNF-*g*-PSBMA not only reduced the foulant attachment on the membrane but also facilitated easy foulant removal from the surface during simple forward washing, thereby increasing the FRR of the CNF-*g*-PSBMA-based TFN membranes.[77]

3.4. Comparison of the Current Work with Literature.

A comparison table (Table 1.) clearly shows that the membrane performance in both FO and RO filtration setups in our current work surpasses that reported in other literature that employed different polymeric materials for TFC membrane performance improvement. Related parameters, such as water and solute flux, pure water permeance, and selectivity, are showcased in the table, confirming the effectiveness of incorporating CNF-*g*-PSBMA in the active layer to achieve our desired goals. The enhancement in membrane performance, particularly in water flux, implies that a larger volume of water can pass through the membrane within a given time. This holds particular significance in large-scale water treatment plants, experiencing a high demand for clean water. In the context of RO filtration, which relies on external pressure for operation, the increased flux is positively correlated to lower-energy consumption. This correlation results in reduced operating and maintenance costs for achieving the same water volume as that of an unmodified membrane.

4. CONCLUSIONS

Modified TFC membranes, with improved water flux, selectivity, and antifouling properties, were created through incorporation of the CNF-*g*-PSBMA polymer into the PA selective layer. Notably, increasing the CNF-*g*-PSBMA concentration up to 100 ppm in TFNs resulted in significant improvements, with TFN-100 showcasing remarkable performance enhancements:

- The membrane water permeation and selectivity in both FO and PRO filtration modes were improved.
- In fouling experiments with BSA and SA, TFN-100 experienced mild water flux decreases of 8 and 10%, respectively. In contrast, unmodified TFC demonstrated sharp flux decline of 35 and 39%, respectively.
- The improved antifouling feature of TFN was predominantly attributed to increased surface hydrophilicity and decreased membrane roughness, as confirmed by AFM.
- TFN-100 exhibited a high FRR, demonstrating its excellent reversible flux recovery capability.

Hence, the proposed modification of the selective PA layer by CNF-*g*-PSBMA provides a reliable and effective method to enhance the FO performance and develop antifouling TFN-FO membranes.

AUTHOR INFORMATION

Corresponding Author

Alireza Shakeri − *School of Chemistry, College of Science, University of Tehran, Tehran 1687794667, Iran;* orcid.org/0000-0003-0730-0412; Email: Alireza.shakeri@ut.ac.ir

Authors

Mehrasa Yassari − *School of Chemistry, College of Science, University of Tehran, Tehran 1687794667, Iran*

Pooria Karami − *Department of Mechanical Engineering, 10-367 Donadeo Innovation Center for Engineering, Advanced Water Research Lab (AWRL), University of Alberta, Edmonton AB T6G 1H9, Canada;* orcid.org/0000-0001-5532-6882

Mohtada Sadrzadeh − *Department of Mechanical Engineering, 10-367 Donadeo Innovation Center for Engineering, Advanced Water Research Lab (AWRL), University of Alberta, Edmonton AB T6G 1H9, Canada;* orcid.org/0000-0002-0403-8351

Complete contact information is available at: https://pubs.acs.org/10.1021/acs.iecr.3c03579

Notes

The authors declare no competing financial interest.

REFERENCES

(1) Mekonnen, M. M.; Hoekstra, A. Y. Four Billion People Facing Severe Water Scarcity. *Sci. Adv.* **2016**, *2*, No. e1500323.

(2) Gude, V. G. Desalination and Water Reuse to Address Global Water Scarcity. *Rev. Environ. Sci. Biotechnol.* **2017**, *16* (4), 591−609.

(3) Anand, A.; Unnikrishnan, B.; Mao, J. Y.; Lin, H. J.; Huang, C. C. Graphene-Based Nanofiltration Membranes for Improving Salt Rejection, Water Flux and Antifouling-A Review. *Desalination* **2018**, *429*, 119−133.

(4) Campione, A.; Gurreri, L.; Ciofalo, M.; Micale, G.; Tamburini, A.; Cipollina, A. Electrodialysis for Water Desalination: A Critical Assessment of Recent Developments on Process Fundamentals, Models and Applications. *Desalination* **2018**, *434*, 121−160.

(5) Noamani, S.; Sadrzadeh, M.; Tehrani-Bagha, A. R. Prospects of Nanocomposite Membranes for Water Treatment by Membrane Distillation. *Nanocomposite Membranes for Water and Gas Separation*; Elsevier, 2020; pp 299−320.

(6) Pan, S. Y.; Haddad, A. Z.; Kumar, A.; Wang, S. W. Brackish Water Desalination Using Reverse Osmosis and Capacitive Deionization at the Water-Energy Nexus. *Water Res.* **2020**, *183*, 116064.

(7) Rastgar, M.; Shakeri, A.; Salehi, H. Study of Polyamide Thin Film Characteristics Impact on Permeability/Selectivity Performance and Fouling Behavior of Forward Osmosis Membrane. *Environ. Sci. Pollut. Res.* **2019**, *26* (2), 1181−1191.

(8) McGinnis, R. L.; Elimelech, M. Energy Requirements of Ammonia-Carbon Dioxide Forward Osmosis Desalination. *Desalination* **2007**, *207* (1−3), 370−382.

(9) Chang, J.; Qiu, H.; Wang, J.; Lin, R.; Hernandez, B. V.; Ji, C.; Liu, G.; Zhao, X.; Ge, L. Efficient Organic Enrichment from Sludge Filtrate via a Forward Osmosis Membrane Process. *J. Environ. Chem. Eng.* **2020**, *8* (4), 104042.

(10) Li, Z.; Wang, Y.; Han, M.; Wang, D.; Han, S.; Liu, Z.; Zhou, N.; Shang, R.; Xie, C. Graphene Oxide Incorporated Forward Osmosis Membranes With Enhanced Desalination Performance and Chlorine Resistance. *Front. Chem.* **2020**, *7* (January), 1−12.

(11) Ahmed, D.; Isawi, H.; Badway, N.; Elbayaa, A.; Shawky, H. Highly Porous Cellulosic Nanocomposite Membranes with Enhanced Performance for Forward Osmosis Desalination. *Iran. Polym. J.* **2021**, *30* (4), 423−444.

(12) Goh, P. S.; Ismail, A. F.; Ng, B. C.; Abdullah, M. S. Recent Progresses of Forward Osmosis Membranes Formulation and Design for Wastewater Treatment. *Water* **2019**, *11* (10), 2043.

(13) Shamaei, L.; Karami, P.; Khorshidi, B.; Farnood, R.; Sadrzadeh, M. Novel Lignin-Modified Forward Osmosis Membranes: Waste Materials for Wastewater Treatment. *ACS Sustain. Chem. Eng.* **2021**, *9* (47), 15768−15779.

Downloaded from pubs.acs.org/iecred/article-pdf/63/1/566/1502927/ie3c03579.pdf by DOKUZ EYLUL UNIV user on 03 September 2026

(14) Dong, X.; Ge, Q. Metal Ion-Bridged Forward Osmosis Membranes for Efficient Pharmaceutical Wastewater Reclamation. *ACS Appl. Mater. Interfaces* **2019**, *11* (40), 37163−37171.
(15) Goh, K. S.; Chen, Y.; Ng, D. Y. F.; Chew, J. W.; Wang, R. Organic Solvent Forward Osmosis Membranes for Pharmaceutical Concentration. *J. Membr. Sci.* **2022**, *642*, 119965.
(16) Wenten, I. G.; Khoiruddin, K.; Reynard, R.; Lugito, G.; Julian, H. Advancement of Forward Osmosis (FO) Membrane for Fruit Juice Concentration. *J. Food Eng.* **2021**, *290*, 110216.
(17) Xiao, S.; Li, Z.; Xiong, Q.; Wu, C.; Huang, J.; Zhou, R.; Jin, Y. Exploration of Sodium Lactate as the Draw Solute of Forward Osmosis for Food Processing. *J. Food Eng.* **2021**, *296*, 110465.
(18) Gonzales, R. R.; Abdel-Wahab, A.; Adham, S.; Han, D. S.; Phuntsho, S.; Suwaileh, W.; Hilal, N.; Shon, H. K. Salinity Gradient Energy Generation by Pressure Retarded Osmosis: A Review. *Desalination* **2021**, *500*, 114841.
(19) Cui, Y.; Liu, X. Y.; Chung, T. S. Enhanced Osmotic Energy Generation from Salinity Gradients by Modifying Thin Film Composite Membranes. *Chem. Eng. J.* **2014**, *242*, 195−203.
(20) Cath, T. Y.; Childress, A. E.; Elimelech, M. Forward Osmosis: Principles, Applications, and Recent Developments. *J. Membr. Sci.* **2006**, *281* (1−2), 70−87.
(21) Gonzales, R. R.; Sasaki, Y.; Istirokhatun, T.; Li, J.; Matsuyama, H. Ammonium Enrichment and Recovery from Synthetic and Real Industrial Wastewater by Amine-Modified Thin Film Composite Forward Osmosis Membranes. *Sep. Purif. Technol.* **2022**, *297*, 121534.
(22) Zhao, X.; Liu, C. Efficient Removal of Heavy Metal Ions Based on the Optimized Dissolution-Diffusion-Flow Forward Osmosis Process. *Chem. Eng. J.* **2017**, *334*, 1128.
(23) Han, G.; Studer, R. M.; Lee, M.; Rodriguez, K. M.; Teesdale, J. J.; Smith, Z. P. Post-Synthetic Modification of MOFs to Enhance Interfacial Compatibility and Selectivity of Thin-Film Nanocomposite (TFN) Membranes for Water Purification. *J. Membr. Sci.* **2023**, *666*, 121133.
(24) Han, G.; Cheng, Z. L.; Chung, T. S. Thin-Film Composite (TFC) Hollow Fiber Membrane with Double-Polyamide Active Layers for Internal Concentration Polarization and Fouling Mitigation in Osmotic Processes. *J. Membr. Sci.* **2017**, *523*, 497−504.
(25) Hakimi, G.; Shakeri, A.; Yassari, M.; Salehi, H. Enhancing the Permeability and Fouling Resistance of Thin-Film Composite Forward Osmosis Membranes via Poly(Ethylene Glycol) Diamine as a Comonomer. *ACS Appl. Polym. Mater.* **2022**, *5*, 567−575.
(26) Han, G.; Zhou, J.; Wan, C.; Yang, T.; Chung, T. S. Investigations of Inorganic and Organic Fouling Behaviors, Antifouling and Cleaning Strategies for Pressure Retarded Osmosis (PRO) Membrane Using Seawater Desalination Brine and Wastewater. *Water Res.* **2016**, *103*, 264−275.
(27) Wang, X.-p.; Hou, J.; Chen, F.-s.; Meng, X.-m. In-Situ Growth of Metal-Organic Framework Film on a Polydopamine-Modified Flexible Substrate for Antibacterial and Forward Osmosis Membranes. *Sep. Purif. Technol.* **2020**, *236*, 116239.
(28) Yassari, M.; Shakeri, A.; Salehi, H.; Razavi, S. R. Enhancement in Forward Osmosis Performance of Thin-Film Nanocomposite Membrane Using Tannic Acid-Functionalized Graphene Oxide. *J. Polym. Res.* **2022**, *29* (2), 43.
(29) Yassari, M.; Shakeri, A.; Salehi, H. ZIF-67 Templated Thin-Film Composite Forward Osmosis Membrane: Importance of Incorporation Method on Morphology and Performance. *Chem. Eng. Res. Des.* **2022**, *180*, 369−378.
(30) Yassari, M.; Shakeri, A. Nature Based Forward Osmosis Membranes: A Novel Approach for Improved Anti-Fouling Properties of Thin Film Composite Membranes. *Chem. Eng. Res. Des.* **2022**, *184*, 137−151.
(31) Bai, L.; Liu, Y.; Bossa, N.; Ding, A.; Ren, N.; Li, G.; Liang, H.; Wiesner, M. R. Incorporation of Cellulose Nanocrystals (CNCs) into the Polyamide Layer of Thin-Film Composite (TFC) Nanofiltration Membranes for Enhanced Separation Performance and Antifouling Properties. *Environ. Sci. Technol.* **2018**, *52* (19), 11178−11187.
(32) Lakra, R.; Balakrishnan, M.; Basu, S. Development of Cellulose Acetate-Chitosan-Metal Organic Framework Forward Osmosis Membrane for Recovery of Water and Nutrients from Wastewater. *J. Environ. Chem. Eng.* **2021**, *9* (5), 105882.
(33) Turbak, A. F.; Snyder, F. W.; Sandberg, K. R. Microfibrillated Cellulose, a New Cellulose Product: Properties, Uses, and Commercial Potential. *J. Appl. Polym. Sci., Appl. Polym. Symp.* **1983**, *37*, 815−827.
(34) Lamm, M. E.; Li, K.; Qian, J.; Wang, L.; Lavoine, N.; Newman, R.; Gardner, D. J.; Li, T.; Hu, L.; Ragauskas, A. J.; Tekinalp, H.; Kunc, V.; Ozcan, S. Recent Advances in Functional Materials through Cellulose Nanofiber Templating. *Adv. Mater.* **2021**, *33* (12), 2005538.
(35) Liu, S.; Low, Z. X.; Hegab, H. M.; Xie, Z.; Ou, R.; Yang, G.; Simon, G. P.; Zhang, X.; Zhang, L.; Wang, H. Enhancement of Desalination Performance of Thin-Film Nanocomposite Membrane by Cellulose Nanofibers. *J. Membr. Sci.* **2019**, *592*, 117363.
(36) Wang, Z. Y.; Xie, F.; Ding, H. Z.; Huang, W.; Ma, X. H.; Xu, Z. L. Effects of Locations of Cellulose Nanofibers in Membrane on the Performance of Positively Charged Membranes. *J. Membr. Sci.* **2022**, *652*, 120464.
(37) Pandey, A. Pharmaceutical and Biomedical Applications of Cellulose Nanofibers: A Review. *Environ. Chem. Lett.* **2021**, *19* (3), 2043−2055.
(38) Vatanpour, V.; Esmaeili, M.; Safarpour, M.; Ghadimi, A.; Adabi, J. Synergistic Effect of Carboxylated-MWCNTs on the Performance of Acrylic Acid UV-Grafted Polyamide Nanofiltration Membranes. *React. Funct. Polym.* **2019**, *134*, 74−84.
(39) Liu, M.; Yu, C.; Dong, Z.; Jiang, P.; Lü, Z.; Yu, S.; Gao, C. Improved Separation Performance and Durability of Polyamide Reverse Osmosis Membrane in Tertiary Treatment of Textile Effluent through Grafting Monomethoxy-Poly(Ethylene Glycol) Brushes. *Sep. Purif. Technol.* **2019**, *209*, 443−451.
(40) Zhang, J.; Wang, Q.; Wang, A. Synthesis and Characterization of Chitosan-g-Poly(Acrylic Acid)/Attapulgite Superabsorbent Composites. *Carbohydr. Polym.* **2007**, *68* (2), 367−374.
(41) Zhang, S.; Ly, Q. V.; Nghiem, L. D.; Wang, J.; Li, J.; Hu, Y. Optimization and Organic Fouling Behavior of Zwitterion-Modified Thin-Film Composite Polyamide Membrane for Water Reclamation: A Comprehensive Study. *J. Membr. Sci.* **2020**, *596*, 117748.
(42) Mahdavi, H.; Rahimi, A. Zwitterion Functionalized Graphene Oxide/Polyamide Thin Film Nanocomposite Membrane: Towards Improved Anti-Fouling Performance for Reverse Osmosis. *Desalination* **2018**, *433*, 94−107.
(43) Zhang, C.; Yuan, J.; Lu, J.; Hou, Y.; Xiong, W.; Lu, H. From Neutral to Zwitterionic Poly(α-Amino Acid) Nonfouling Surfaces: Effects of Helical Conformation and Anchoring Orientation. *Biomaterials* **2018**, *178*, 728−737.
(44) Zhang, C.; Lu, J.; Hou, Y.; Xiong, W.; Sheng, K.; Lu, H. Investigation on the Linker Length of Synthetic Zwitterionic Polypeptides for Improved Nonfouling Surfaces. *ACS Appl. Mater. Interfaces* **2018**, *10* (20), 17463−17470.
(45) Sedghi, R.; Heidari, B.; Yassari, M. Novel molecularly imprinted polymer based on β -cyclodextrin@graphene oxide: Synthesis and application for selective diphenylamine determination. *J. Colloid Interface Sci.* **2017**, *503*, 47−56.
(46) Zhao, C.; Xue, J.; Ran, F.; Sun, S. Modification of Polyethersulfone Membranes - A Review of Methods. *Prog. Mater. Sci.* **2013**, *58* (1), 76−150.
(47) Chen, W.; Yu, H.; Liu, Y.; Hai, Y.; Zhang, M.; Chen, P. Isolation and Characterization of Cellulose Nanofibers from Four Plant Cellulose Fibers Using a Chemical-Ultrasonic Process. *Cellulose* **2011**, *18* (2), 433−442.
(48) Morán, J. I.; Alvarez, V. A.; Cyras, V. P.; Vázquez, A. Extraction of Cellulose and Preparation of Nanocellulose from Sisal Fibers. *Cellulose* **2008**, *15* (1), 149−159.
(49) Soni, B.; Hassan, E. B.; Mahmoud, B. Chemical Isolation and Characterization of Different Cellulose Nanofibers from Cotton Stalks. *Carbohydr. Polym.* **2015**, *134*, 581−589.

Downloaded from pubs.acs.org/iecred/article-pdf/63/1/566/1502927/ie3c03579.pdf by DOKUZ EYLUL UNIV user on 03 September 2026

https://doi.org/10.1021/acs.iecr.3c03579
Ind. Eng. Chem. Res. 2024, 63, 566−578

(50) Guo, Z.; Pereira, T.; Choi, O.; Wang, Y.; Hahn, H. T. Surface Functionalized Alumina Nanoparticle Filled Polymeric Nanocomposites with Enhanced Mechanical Properties. *J. Mater. Chem.* **2006**, *16* (27), 2800−2808.
(51) Ren, P. F.; Yang, H. C.; Liang, H. Q.; Xu, X. L.; Wan, L. S.; Xu, Z. K. Highly Stable, Protein-Resistant Surfaces via the Layer-by-Layer Assembly of Poly(Sulfobetaine Methacrylate) and Tannic Acid. *Langmuir* **2015**, *31* (21), 5851−5858.
(52) Canché-Escamilla, G.; De los Santos-Hernández, J.; Andrade-Canto, S.; Gómez-Cruz, R. Obtención de Celulosa a Partir de Los Desechos Agrícolas Del Banano. *Inf. Tecnol.* **2005**, *16* (1), 83−88.
(53) Lalani, R.; Liu, L. Synthesis, Characterization, and Electrospinning of Zwitterionic Poly(Sulfobetaine Methacrylate). *Polymer (Guildf).* **2011**, *52* (23), 5344−5354.
(54) Vilela, C.; Moreirinha, C.; Domingues, E. M.; Figueiredo, F. M. L.; Almeida, A.; Freire, C. S. R. Antimicrobial and Conductive Nanocellulose-Based Films for Active and Intelligent Food Packaging. *Nanomaterials* **2019**, *9* (7), 980.
(55) Ip, M.; Wirjosentono, B.; Tamrin; Ja, M.; Mendez, J. A. Thermal and Morphology Properties of Cellulose Nanofiber from TEMPO-Oxidized Lower Part of Empty Fruit Bunches (LEFB). *Open Chem.* **2019**, *17* (1), 526−536.
(56) Georgouvelas, D.; Jalvo, B.; Valencia, L.; Papawassiliou, W.; Pell, A. J.; Edlund, U.; Mathew, A. P. Residual Lignin and Zwitterionic Polymer Grafts on Cellulose Nanocrystals for Antifouling and Antibacterial Applications. *ACS Publ.* **2020**, *2* (8), 3060−3071.
(57) Sosiati, H.; Wijayanti, D. A.; Triyana, K.; Kamiel, B. Morphology and Crystallinity of Sisal Nanocellulose after Sonication. *AIP Conference Proceedings*; AIP Publishing, 2017; Vol. *1877*.
(58) Dufresne, A.; Cavaillé, J. Y.; Vignon, M. R. Mechanical Behavior of Sheets Prepared from Sugar Beet Cellulose Microfibrils. *J. Appl. Polym. Sci.* **1997**, *64* (6), 1185−1194.
(59) Khorshidi, B.; Thundat, T.; Fleck, B. A.; Sadrzadeh, M. A Novel Approach Toward Fabrication of High Performance Thin Film Composite Polyamide Membranes. *Sci. Rep.* **2016**, *6* (1), 22069.
(60) Ren, J.; McCutcheon, J. R. A New Commercial Thin Film Composite Membrane for Forward Osmosis. *Desalination* **2014**, *343*, 187−193.
(61) Sadrzadeh, M.; Hajinasiri, J.; Bhattacharjee, S.; Pernitsky, D. Nanofiltration of Oil Sands Boiler Feed Water: Effect of PH on Water Flux and Organic and Dissolved Solid Rejection. *Sep. Purif. Technol.* **2015**, *141*, 339−353.
(62) Sadrzadeh, M.; Pernitsky, D.; McGregor, M. Nanofiltration for the Treatment of Oil Sands-Produced Water. *Nanofiltration*; InTech Rijeka, 2018.
(63) Ghosh, A. K.; Jeong, B. H.; Huang, X.; Hoek, E. M. V. Impacts of Reaction and Curing Conditions on Polyamide Composite Reverse Osmosis Membrane Properties. *J. Membr. Sci.* **2008**, *311* (1−2), 34−45.
(64) Baroña, G. N. B.; Lim, J.; Choi, M.; Jung, B. Interfacial Polymerization of Polyamide-Aluminosilicate SWNT Nanocomposite Membranes for Reverse Osmosis. *Desalination* **2013**, *325*, 138−147.
(65) Li, H.; Shi, W.; Zhang, Y.; Du, Q.; Qin, X.; Su, Y. Improved Performance of Poly(Piperazine Amide) Composite Nanofiltration Membranes by Adding Aluminum Hydroxide Nanospheres. *Sep. Purif. Technol.* **2016**, *166*, 240−251.
(66) Shakeri, A.; Salehi, H.; Ghorbani, F.; Amini, M.; Naslhajian, H. Polyoxometalate Based Thin Film Nanocomposite Forward Osmosis Membrane: Superhydrophilic, Anti-Fouling, and High Water Permeable. *J. Colloid Interface Sci.* **2019**, *536*, 328−338.
(67) Haresco, C. K. S.; Ang, M. B. M. Y.; Doma, B. T.; Huang, S. H.; Lee, K. R. Performance Enhancement of Thin-Film Nanocomposite Nanofiltration Membranes via Embedment of Novel Polydopamine-Sulfobetaine Methacrylate Nanoparticles. *Sep. Purif. Technol.* **2021**, *274*, 119022.
(68) Mi, B.; Elimelech, M. Organic Fouling of Forward Osmosis Membranes: Fouling Reversibility and Cleaning without Chemical Reagents. *J. Membr. Sci.* **2010**, *348* (1−2), 337−345.
(69) Lu, X.; Castrillón, S. R. V.; Shaffer, D. L.; Ma, J.; Elimelech, M.; Elimelech, M. In Situ Surface Chemical Modification of Thin-Film Composite Forward Osmosis Membranes for Enhanced Organic Fouling Resistance. *ACS Publ.* **2013**, *47* (21), 12219−12228.
(70) Liao, C.; Zhao, J.; Yu, P.; Tong, H.; Luo, Y. Synthesis and Characterization of SBA-15/Poly (Vinylidene Fluoride) (PVDF) Hybrid Membrane. *Desalination* **2010**, *260* (1−3), 147−152.
(71) Ghaemi, N.; Madaeni, S. S.; Daraei, P.; Rajabi, H.; Zinadini, S.; Alizadeh, A.; Heydari, R.; Beygzadeh, M.; Ghouzivand, S. Polyethersulfone Membrane Enhanced with Iron Oxide Nanoparticles for Copper Removal from Water: Application of New Functionalized Fe3O4 Nanoparticles. *Chem. Eng. J.* **2015**, *263*, 101−112.
(72) You, X.; Ma, T.; Su, Y.; Wu, H.; Wu, M.; Cai, H.; Sun, G.; Jiang, Z. Enhancing the Permeation Flux and Antifouling Performance of Polyamide Nanofiltration Membrane by Incorporation of PEG-POSS Nanoparticles. *J. Membr. Sci.* **2017**, *540*, 454−463.
(73) Liu, X.; Ng, H. Y. Fabrication of Layered Silica-Polysulfone Mixed Matrix Substrate Membrane for Enhancing Performance of Thin-Film Composite Forward Osmosis Membrane. *J. Membr. Sci.* **2015**, *481*, 148−163.
(74) Phillip, W. A.; Yong, J. S.; Elimelech, M. Reverse Draw Solute Permeation in Forward Osmosis: Modeling and Experiments. *Environ. Sci. Technol.* **2010**, *44* (13), 5170−5176.
(75) Zhu, J.; Zhou, S.; Li, M.; Xue, A.; Zhao, Y.; Peng, W.; Xing, W. PVDF Mixed Matrix Ultrafiltration Membrane Incorporated with Deformed Rebar-like Fe3O4-Palygorskite Nanocomposites to Enhance Strength and Antifouling Properties. *J. Membr. Sci.* **2020**, *612*, 118467.
(76) Shen, L.; Yi, M.; Tian, L.; Wang, F.; Ding, C.; Sun, S.; Lu, A.; Su, L.; Wang, Y. Efficient Surface Ionization and Metallization of TFC Membranes with Superior Separation Performance, Antifouling and Anti-Bacterial Properties. *J. Membr. Sci.* **2019**, *586*, 84−97.
(77) Mazlan, N. M.; Marchetti, P.; Maples, H. A.; Gu, B.; Karan, S.; Bismarck, A.; Livingston, A. G. Organic Fouling Behaviour of Structurally and Chemically Different Forward Osmosis Membranes - A Study of Cellulose Triacetate and Thin Film Composite Membranes. *J. Membr. Sci.* **2016**, *520*, 247−261.
(78) Song, X.; Wang, L.; Tang, C. Y.; Wang, Z.; Gao, C. Fabrication of Carbon Nanotubes Incorporated Double-Skinned Thin Film Nanocomposite Membranes for Enhanced Separation Performance and Antifouling Capability in Forward Osmosis Process. *Desalination* **2015**, *369*, 1−9.
(79) Gyanwali, G.; Hodge, M.; White, J. L. Cyclodextrin Functionalization: Simple Routes to Tailored Solubilities and Nanoscopic Polymer Networks. *J. Polym. Sci. Part A Polym. Chem.* **2012**, *50* (16), 3269−3276.
(80) Nguyen, T.; Roddick, F. A.; Fan, L. Biofouling of Water Treatment Membranes: A Review of the Underlying Causes, Monitoring Techniques and Control Measures. *Membr.* **2012**, *2* (4), 804−840.

NOTE ADDED AFTER ASAP PUBLICATION

This paper was originally published ASAP on December 30, 2023. Due to a production error, there was a typo in the first two authors' surnames. The corrected version reposted on January 10, 2024.

Downloaded from pubs.acs.org/iecred/article-pdf/63/1/566/1502927/ie3c03579.pdf by DOKUZ EYLUL UNIV user on 03 September 2026

https://doi.org/10.1021/acs.iecr.3c03579
Ind. Eng. Chem. Res. 2024, 63, 566−578